

First of its Kind: A Test Artifact for Direct Laser Writing

Sven Fritzsche^{1,†}, Brian R. Pauw¹, Christiane Weimann¹, Heinz Sturm¹

¹ Bundesanstalt für Materialforschung und -prüfung, Unter den Eichen 87, 12205 Berlin, Germany

E-mail: sven.fritzsche@bam.de

† Corresponding author

Abstract. With Direct Laser Writing (DLW) maturing in all aspects as a manufacturing technology a toolset for quality assurance must be developed. In this work we want to introduce a first of its kind test artifact. Test artifacts are standardized 3D models with specific geometric feature to evaluate the performance of writing parameters. Test artifacts are already common in other 3D additive manufacturing technologies e.g. Selective Laser Melting. The test artifact introduced in this work was developed in particular to accommodate 1) the high geometrical resolution of DLW structures and 2) the limited possibilities to examine the resulting structure. Geometric accuracy, surface adhesion as well as confocal raman spectroscopy results were considered when evaluating the design of the test artifact. We will explain the individual features and design considerations of our DLW test artifact. The difference between two slicers, Cura and 3DPoli, and the implications on measured feature sizes and the general shape is quantified. The measured geometries are used to derive a general design guide for a specific combination of photoresist, laser power and scanning speed and to analyse the geometric accuracy of a structure produced using these guidelines.

Keywords— test artifact; two photon polymerization; Direct Laser Writing; quality infrastructure; multi photon lithography

Introduction

Direct Laser Writing via two-photon polymerization (2PP) or multi-photon lithography (MPL) has matured towards a versatile manufacturing technology. The fabricated objects range from a few micrometer [1] to centimeters in size. The feature size of these objects can be in the sub-micron range depending on multiple parameters. [2] Only with a coordinated orchestration of positioning tables, optical components and the appropriate control parameters, as well as suitable control software, can an exact replica with the desired properties be fabricated. A wide range of different applications would benefit from the use of test artifacts biomedical applications [3–5], optical elements [6–8] or microfluidic [9, 10] objects fabricated in-place as well as reference structures for roughness measurements [11, 12]. In fact, these processes would also have to be coordinated with the materials used, such as hybrid polymers [13], biocompatible hydrogels [14, 15] and ceramics [16]. Also ageing effects on hybrid polymers have been studied [17].

The wide range of proposed applications show the need of a quality assurance tool case for DLW. Test artifacts are 3D models with a certain set of features (e.g. geometrical, device-specific or technique-specific) that can be evaluated after the fabrication step. In other 3D Fabrication techniques like Selective Laser Melting/Sintering (SLM/SLS), test artifacts are already used to determine the quality of the test artifact itself and the current state of the machine such as the general additive manufacturing test artifact introduced by Moylan [18] in 2014. A highly-integrated test artifact that considers mechanical, geometrical as well as chemical analysing methods was shown by Taylor [19]. Similar artifacts have also been shown for polymer additive manufacturing [20]. Due to the different material and technology used for the mentioned test artifacts, portability of these existing artifacts to DLW is not feasible, whereas the general usefulness of a test artifact for DLW will be examined in this study.

To fabricate complex three-dimensional structures based on a given 3D model the use of a slicing software is needed. Generally, slicers split a model perpendicular to the fabrication direction into layers or “slices” with a certain slicing distance d_z . To rapidly polymerize the solid parts of a slice, defined by its outer and inner contours by straight or curved lines, a “hatching” process is used. The distance between each parallel line in a slice is called hatching distance d_h . An optimisation strategy must be determined: If the hatch distance is too large, the volume within the voxel may not be fully polymerized, but the fabrication time will be reduced. If the spacing is small, resulting in partial overlapping of exposure positions, this improves curing and costs time but can also lead to degradation effects [7, 21] and increases fabrication time. The cause of the dilemma is ultimately that the smallest volumes (voxels) are not cubes or cuboids that fit together perfectly in three dimensions and that are cured homogeneously. Nevertheless, this approach is and must be the basis of the digitally controlled guidance of the laser focus. Different studies on slicing approaches regarding DLW technique have been conducted

[22–24]. Bauer et al. [25] investigated the relationship between laser velocity, laser power and hatch/slice distance and found a mechanical enhancing effect at higher overlaps. On the other hand, an increase in size was also observed for SZ080, which also depended on the manufacturing direction [26].

In this paper, we first present the test artifact we devised and explain the rationale for its design in terms of the DLW technique. We then qualify and quantify the test artifact, which was initially made from an SZ2080 photoresist. We perform a comparison between two different slicer software variants and explain the impact on geometrical aspects as well as on the general shape of the test artifact. In the last section, we use the geometric information as general design guidelines for optimized structures with more accurate geometric dimensions.

1. Experimental

1.1. MPLS platform

Fabrication of the test artifact was performed using a LaserNanofactory by Femtika, Lithuania, which incorporates a laser light source C-Fiber 780 High Power (Menlo Systems GmbH) operating at 100 fs pulse duration, 100 MHz repetition rate and 780 nm wavelength. The used immersion oil objective was a Zeiss Plan-Apochromat with a $63\times$ magnification and a numerical aperture of 1.4. For machine control software used was 3DPoli v6.33 by Femtika.

The used photoresists in this work are SZ2080 obtained from FORTH (Heraklion/Greece) and OrmoComp obtained from MicroResist GmbH (Berlin/Germany).

1.2. Light microscopy Electron microscopy

1.3. Micro Raman Microscopy

Confocal Raman measurements were performed with a confocal Alpha300R instrument (WITec, Germany), equipped with a $20\times$ Zeiss EX Epiplan DIC objective, a 532 nm laser (Excelsior 532-60) with a laser power of up to 20 mW. The spectrometer was an UHTS-300-VIS with two different gratings (pls. see below) and an thermoelectrically cooled CCD-camera Andor DV-401A-BV-532 at -64°C .

For overview scans, a blazed grating called T1 with 600 grooves/mm was used, which is optimized for 500 nm and allows a scan up to a wavenumber of about 3800 cm^{-1} . In this case, a spectral resolution of three wavenumbers is achieved in combination with a CCD camera with 1024 pixels. The laser intensity at 532 nm, which corresponds to a relative wavenumber of zero, is attenuated by several decades by an edge filter, but is usually still visible. Peak positions and peak widths are evaluated and serve to assess the quality of the spectrum over time. For a higher spectral resolution with an identical camera, the grating called T3 with 1800 grooves/mm (500 nm) offers a resolution of about one wavenumber, reducing the width of the possible scan to about one third.

The instrument works in reflection mode. A glass fibre with a core diameter of 100 μm serves as the aperture of the spectrometer in the confocal setup. To reduce the local load on the sample surface, as large an area as possible of the designated square of the test artifact is scanned so that no local spot is burnt in. Wider scan fields include the substrate at the edge. Since the spectra of the test square show spectral bands of the glass substrate, these glass spectra can be used for the weighted subtraction.

2. A new test artifact for MPLS

2.1. Features (regions and properties)

The test artifact described here was optimized for a DLW configuration that uses an immersion oil objective with an NA of 1.4 and a photoresist with a voxel size below 2 μm though it is easily adapted to other configurations through uniform scaling. Groups of individual components of the test artifact that, together, serve a calibration or test function are called “features”. The design of the test artifact follows the general construction guidelines on test artifacts for additive manufacturing, which were published by NIST in 2012.

The requirements for these were laid out by Moylan et al. [27], as:

- be large enough to test the performance of the machine near the extremes of the platform as well as near the center,
- have a substantial number of small, medium, and large features,
- have both holes and bosses to aid in verifying beam width compensation,
- not take too long to build,
- not consume a large quantity of material,
- be easy to measure, and
- have many features of a real part (i.e., thin walls, flat surfaces, holes, etc.)

It was also pointed out by Byun[28] that 1) the minimum feature size should be determined, and 2) the features should be distributed on several axes in order to observe dependencies on the manufacturing location or direction. Since the scale of DLW structures is much smaller than the test artifacts previously described for SLM/SLS additional guidelines should be developed for DLW test artifacts. Post-processing of the DLW test artifact produced according to the procedures defined in this paper should ideally be limited to the addition of a conductive coating if necessary for scanning electron microscopy (SEM). This can be avoided altogether if the artifact is solely examined with optical microscopy (OM).

A variety of constraints have to be taken into consideration at the design of the test artifact. In the following we want to outline them. The minimum feature size, but also the shape of the voxel, and thus the resolution of the DLW method is greater in the lateral direction than axial to the writing laser beam [29]. With lower NA

the axial resolution of DLW structures decreases more than in lateral direction. The determination of resolution perpendicular to the substrate can be problematic because in SEM and OM the sample must be tilted, leading to distortions. When viewing from the side, large substrates can be a hindrance to imaging; yet cutting them off risks jeopardizing the fabricated structure. With DLW, features can be present that are of such small dimensions that they fall below the detectability of the OM [30], here confocal OM or scanning probe microscopy (AFM) may offer themselves as a possible solution. In the production of the test artifacts, the field of view (FOV) of the lens used for exposure plays a role, a feature that is also coupled to the magnification of the lens. To produce objects that are larger than the area accessible in the FOV, one must either work sequentially with partially overlapping fabrication areas (stitching) or use a so-called Infinite Field of View (IFOV) principle (cf. [31]). The IFOV principle combines the galvanic scanners with a servo stage for the purpose of a combined scanning movement. The boundary conditions derived therefrom for the construction of the artifact were determined as shown in Table 1.

Table 1: Additional Constraints on DLW test artifact design

Constraint	Reason
Lateral Size	has to be larger than field of view
Height	limitation of fabrication time
Distances between Features	minimal distance of 5 μm between each feature
Bulk/Non-Bulk	Surface attachment of bulk and non-bulk parts can be compared
Immersion indicator	degree of immersion can be estimated
Feature sizes	based on Reynards series following ISO 3 [32], similar for key features

The individual features of the test artifact are shown in Figure 1 and further explained in Table 2.

The outer ring feature (#1) is a ring with a diameter of 400 μm and a height/width of 5 μm . The ring thus expands outside of the FOV of the lens, thus testing the interaction of multiple stages or stitching method used for writing larger structures. In addition, information about the tilt of the substrate can be obtained, as tilting changes the height of the ring locally; with heavily tilted substrates, part of the ring may even disappear or delaminated, since the laser focal point is completely incorporated into the substrate.

The version indicator (#2) is used to differentiate between the current and upcoming versions of the test artifact.

The "Z spacing" feature (cf. Figure 2) (#3) consists of 12 identical bars, which are placed freely in space without binding to the gate above. The free distance between the bars and the gate starts at 1 μm (Figure 2, light grey left side) and increases in 0.5 μm steps to a maximum of 5.5 μm (dark grey, far right). Since the cross-linked voxel can be approximated as a rotational ellipsoid with high expansion in the Z-direction, an

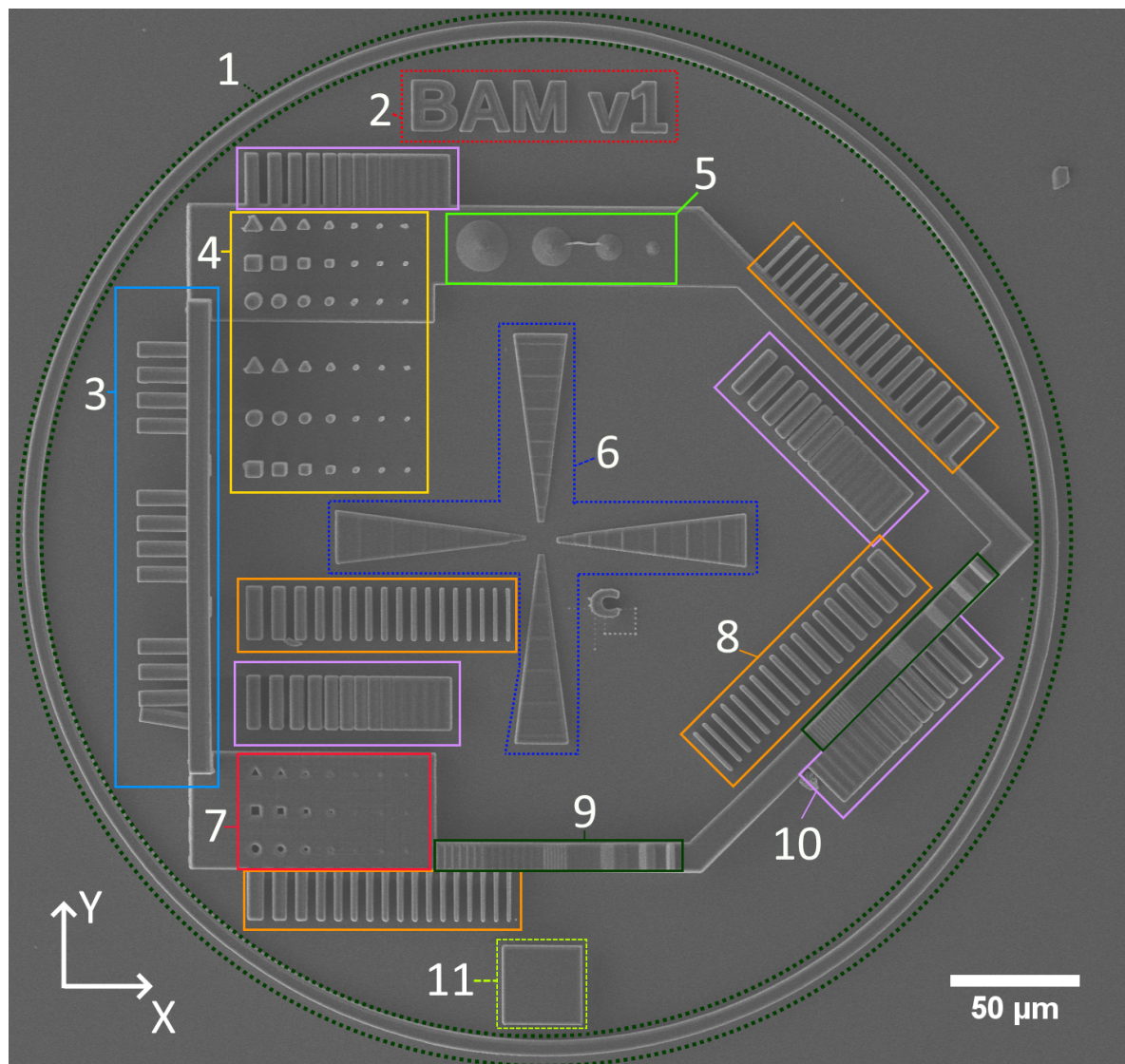


Figure 1: Overview SEM image of a test artifact with highlighted features as shown in Table 2, fabricated with SZ2080, 12 mW Laser Power and a velocity of $7000 \mu\text{m/s}$, d_h $0.2 \mu\text{m}$, d_z $0.2 \mu\text{m}$, indicated features are described in Table 2

unintentional solid connection occurs at a distance of $1 \mu\text{m}$ from the portal. The reason is that both the height of the free bar and the height of the portal are larger than defined in the fabrication script due to the added voxel height. As the distance increases, the connection between the bar and the gate is reduced to a thin thread, which leads to a dislocation of the bar or even to a detachment from the gate when the stabilising monomer gel is washed away during the development process. This makes it possible to estimate the vertical fabrication precision, and the overlap of the successive layers, respectively.

The Rods feature (#4) consists of triplets of shaped rods with a height of $20 \mu\text{m}$ of decreasing lateral dimension. Each triplet consists of a square, triangular and round

Table 2: Naming of individual features of artifact as shown in Figure 1

Number	Feature
1	Outer Ring
2	Version Indicator
3	Z spacing
4	Rods
5	Cones
6	Immersion indicator
7	Holes
8	Thin Walls
9	Staircase Control
10	Gaps
11	Test Pad

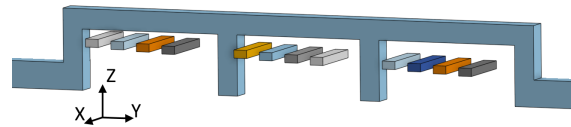


Figure 2: Tilted CAD view of the "Z spacing" feature (#3) with the top portal and two pillars (blue), the 12 unattached bars with increasing space from left to right are placed underneath and shown in different colours

rod, with similar lateral chord lengths. The rods are placed once directly onto the substrate and once on a base body to observe the influence of substrate adhesion. With the reduced chord lengths, the accuracy of reproducing geometric shapes at smaller diameters can be estimated. The corresponding feature #7 has the same shape as the rods in the bulk body and can be used to estimate the replicability of fabricating negative shapes in the XY plane.

The cone feature (#5) placed on the bulk body consists of four spherical cones with an angle of 45° and a diameter of 5 to 20 μm in 5 μm -steps. Due to the slicing process each cone will be separated in circles with a decreasing diameter. The feature can be used to observe the shutter properties as for each circle the shutter has to be opened and closed at precise locations. Deformations along these cones are possible due to problems with the shutter timing or the chosen slicing profile.

To find out how well the test object is connected to the substrate in comparison with the preset printing depth, the immersion indicator (#6) is positioned in the centre of the artifact. This consists of four wedges whose height decreases towards the centre. With a length of 80 μm and a maximum height of 5 μm , a very low incline ($\approx 3.6^\circ$) is obtained and the object is thus very sensitive to the starting depth of writing on the substrate. Therefore, if e.g. only half of the Immersion Indicator is visible the

whole test artifact has been fabricated about $2.5\ \mu\text{m}$ into the substrate. To ensure intercomparability between test artifacts we propose that the maximal immersion is less than $2.5\ \mu\text{m}$, which corresponds to a distance between the remaining Immersion Indicator wedges of $80\ \mu\text{m}$. It must be noted that the wedges are not angled towards the substrate due to the staircase effect and therefore the distance between the individual steps depends on the slicing height. Using e.g. an AFM or confocal OM, a determination of the thickness of a sliced plane easily determined. Figure 3 shows the effect and resulting shape.

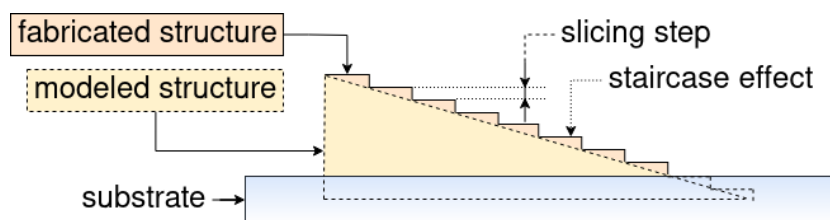


Figure 3: Schematic Illustration of staircase effect and resulting structure

The Thin Walls (#8) and Gaps features (#10) are used to assess the geometrical accuracy of the system. Both features are either freestanding or attached to the bulk body to examine the influence of the substrate and for the attached features the influence of the slicing method. Both features are additionally fabricated at a 45° angle to observe the diagonal feature precision.

The staircase feature (#9) consists of five pyramids with a height of $5\ \mu\text{m}$ on top of the bulk body. Their angle is gradually increased by 15° from 15° to a maximum of 75° . The feature is repeated in a 45° angle on the bulk body for the influence of non-perpendicular features have on the staircase effect.

The Test pad feature (#11) is a simple cubic structure with a side length of $30\ \mu\text{m}$ and a height of $10\ \mu\text{m}$. It can be used for methods such as confocal raman spectroscopy, micro-indentation or white light interferometry to analyse chemical, mechanical or structural properties.

2.2. Test Pad evaluation via Confocal Raman Spectroscopy

The effect of light intensity during the writing process and possible post-curing by daylight changes the cross-linking density of the fabricated structure. This can affect the dimensional stability of the structure and its optical and mechanical properties. Therefore, the test pad feature is evaluated via micro raman microscopical comparing of two test pads fabricated with $12\ \text{mW}$ and $18\ \text{mW}$ of writing laser power, respectively. First, the chemical composition, the curing reaction and the assignment of the raman peaks to the different chemical groups is discussed. Then it is shown that it is possible to follow the progress of the photoreaction under exposure to the fs laser at $780\ \text{nm}$.

Raman experiments with SZ2080 photoresist failed due to the dominance of fluorescence over the raman intensities, so here only the OrmocompTM photoresist is used

and evaluated as a model system. A description of the Ormocomp™ precursor or network is unfortunately not clearly described in literature, only the dissertation by S. Obi [33] contains corresponding information in the form of a structural formula. The formula given there shows a chain based on -O-Si-O-Si units to which polymerizable side groups are attached. This side group starts with a propanethiol as a spacer to the silicate chain and branches into a three-armed structure. This in turn consists of a quaternary carbon atom with three attached structural elements of acrylic acid and an ethyl group. Two still reactive vinyl groups of the acrylic acid remain in the structural unit, the third served for the connection to the spacer (see Figure 4). It is not certain that the description of the precursor is complete, but further information could not be obtained. To the best of our knowledge, no information is known about any photoactivators or other additives in the Ormocomp formulation used. The incomplete information nevertheless provides an important guidance with regard to the interpretation of the Raman spectra.

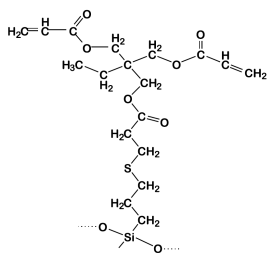


Figure 4: Chemical composition of the precursor of Ormocomp, after S. Obi [33]

Figure 5 shows raman overview spectra of the photocurable resin after exposure with different power, 12 mW and 18 mW. After taking into account the raman response of the glass substrate and a background correction, the spectra are almost congruent with each other. A calculation of two weighted differences of the spectra shows the deviations more clearly (Figure 5 d, e).

Only a few literature references could be found for the assignment of Raman peaks to chemical groups. Raman spectra of Ormocomp describing the 2PP process in the range 1400-1800 cm^{-1} can be found in Rys et al. [34] with a spectral resolution estimated at 1 cm^{-1} . Spectra from literature often show spectral ranges for the groups and only rarely sharp peaks. This is due to the chemical environment of the groups. The range around 1630 cm^{-1} is assigned to the reactive ($\text{H}_2\text{C}=\text{CH}-$) double bond, a group whose concentration and thus signal strength decreases with progressive photopolymerization. In the spectra, additionally, a strong peak at $\approx 1740 \text{ cm}^{-1}$ appears [35], which is related to the carbonyl bond ($\text{O}=\text{C}-$), as also found in [34]. The difference spectra show two main areas of deviation in form of positive peaks at ≈ 1630 and $\approx 2900\text{-}3100 \text{ cm}^{-1}$. Positive peaks mean that the concentration of the associated group was even greater at 12 mW exposure strength than after 18 mW power input. Conversely, this means that photocuring with the fs pulse laser consumes these groups. In Figure 5 e), a negative peak for carbonyl ($\approx 1740 \text{ cm}^{-1}$) is found additionally. Let us not forget that the recording of

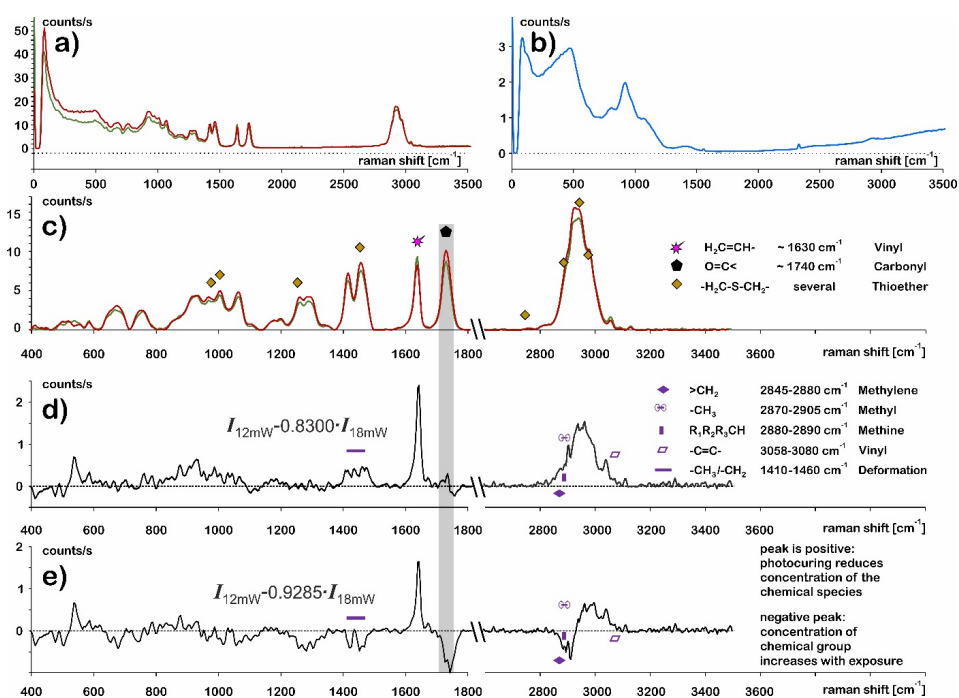


Figure 5: Raman spectra of Ormocomp™ (a, c) and the glass substrate (b) as well as two difference spectra (d, e) of a photo-curing in the femtosecond laser printer at 1080 nm, measured with grating T1 (3 cm^{-1}). a) Raw data spectrum after printing process with 12 mW line power of the laser (green line) and with 18 mW (red line). A comparison with the spectrum of the glass substrate in b) shows the necessity of a weighted subtraction, result shown in c). The difference spectrum (d, e) positively weights the data at 12 mW and subtracts from it the curve belonging to 18 mW. The weighting factor of ≈ 0.83 in (d) was chosen under the assumption that the concentration of carbonyl bonds remains constant during light curing and ageing and that therefore the difference of the two spectra at the grey marked position should be as close to zero as possible. The weighting factor of 0.9285 in (e) was chosen so that the sum of all intensities is zero.

the two spectra required a change of sample, whereupon a new positioning of the focal distance must be made in confocal microscopy spectroscopy. For this reason, the slight differences in the spectra caused by this must be compensated for by a method that requires knowledge of the molecular groups, their band position and the most probable chemical reaction that has just been worked out. If the difference of the spectral intensity $I(v)_{12mW} - f \cdot I(v)_{18mW}$ is formed and the intensities for the peak at 1740 cm^{-1} (carbonyl) are minimized, $f = 0.83$ applies. If the sum of all intensities is compensated to zero, the correction factor $f = 0.9285$ and leaves a negative peak in the carbonyl range.

Let us first inspect Figure 5 d) more closely. If we look at the peaks in the spectra in Figure 5 c), we see that the result of the difference formation in the range between $600 - 1500 \text{ cm}^{-1}$ is not very clear. The differences are always small and noise strongly, which reduces their significance. Only a few peaks can be unambiguously assigned, e.g., the positions marked with a yellow rhombus could belong to thioether

linkages of various kinds [36], but their assignment is not certain. We refrain from an interpretation. Assuming that the chemical composition of OrmoComp given in Figure 4 is correct and in particular complete, only the vinyl groups ($\text{H}_2\text{C}=\text{CH}-$) should be involved in the photoreaction with the fs-laser light. An analogue is the reaction of acrylic acid to polyacrylic acid, which proceeds via a radical mechanism. In this case, the concentration of the carbonyl groups ($\text{O}=\text{C}-$) does not change and a weighting factor of 0.83 fulfils this condition for the peak at $\approx 1740\text{ cm}^{-1}$ as well as possible. Consequently, the difference peak at 1630 cm^{-1} is positive because the concentration of the vinyl group decreases with stronger exposure. The only other meaningful area is the range between $2800 - 3100\text{ cm}^{-1}$. It contains the most diverse chemical groups and is difficult to evaluate with a structure that is not completely known. Nevertheless, it should be recognisable that the vinyl group ($3058 - 3080\text{ cm}^{-1}$) is consumed, this is true, the peak is positive. Obviously, many other species are also consumed, but according to the reaction scheme, some of them should be formed. For example, one methine group or methanetriyl group ($>\text{CH}-$) and one methylene bridge (methanediyl group, $-\text{CH}_2-$) are formed per reacted vinyl group ($\text{H}_2\text{C}=\text{CH}-$) at the acrylic end. There, the difference should be negative, which is obviously not the case in Figure 5 d). According to the state of knowledge about the compound, this cannot be the case, which makes the first choice of the weighting factor not plausible. However, this also means that the idea of the non-participation of the carbonyl group in the photoreaction must be abandoned. Figure 5 e), on the other hand, shows a difference spectrum with a weighting factor of 0.9285 that gives the value zero as the sum of all intensities. It is 12% higher than the value in Figure 5 d). In this case, the range between 2800 and 3100 cm^{-1} splits into a positive (species are consumed) and a negative (species are produced) range. It is understandable that methylene groups ($2845 - 2880\text{ cm}^{-1}$) and methine groups ($2880 - 2890\text{ cm}^{-1}$) [35] are generated when the vinyl group reacts. The generation of methyl groups ($2870 - 2890\text{ cm}^{-1}$) neither fits to the chain generation nor to the termination reactions of a radical polymerisation of acrylic acid. In contrast, however, the deformation oscillation of the methylene group ($1410 - 1460\text{ cm}^{-1}$) also appears as a negative peak, which correctly corresponds to the result of the polymerisation. The range between 2930 and 3080 cm^{-1} reflects the consumed species, the vinyl group lies in this range, but the assignment of the remaining raman bands is unknown. It is clearly visible, however, that a negative peak is formed at 1740 cm^{-1} , i.e., carbonyl groups should be formed. Reaction pathways could be found for this, but not proven within the scope of this work. For example, one would have to assume the participation of atmospheric oxygen in the photocuring process. A possible reaction with oxygen can be well justified: The existing pre-polymerisation via the silicate chain, which is present in the precursor, leads to a steric hindrance at the reactive vinyl group.

If these are activated radically, they need sufficient proximity to the next vinyl group. If this cannot be achieved, the activated chain ends can only be saturated with oxygen, which explains the generation of carbonyl groups with increasing exposure.

In the future, photopolymerisation with the exclusion of oxygen is being considered,

but this would involve some effort.

It remains to be noted that the degree of curing by the fs laser can be determined by means of Raman microspectroscopy on an appropriately constructed test artefact.

In this case it would be advantageous to avoid signal components of the substrate, because finding the correct weighting factor is not error-free. One solution would be to increase the thickness of the object at the landing site intended for Raman measurement. A lens with a higher magnification and a shorter focus length could also be used.

Post-curing reaction induced by laser beam exposure: Synthesis and degradation The further cured sample (fs-laser 780 nm at 18 mW, see difference spectrum in Figure 5) was further investigated with the aim of determining its stability. Further formation of the networks during visible light exposure can alter dimensional stability, adhesion to the substrate and mechanical properties. The laser of the raman microscope (532 nm) serves as a light source and exposes a spot with a diameter of 3 to 4 μm . The use of polarized light opens up greater sensitivity to change as the orientation of the groups changes. Exposure for an additional 14 h was used to investigate whether further changes occur at this already pre-cured position. Since the wavelength of 532 nm (corresponds to 2.33 eV) used for Raman measurements is about as high as the energy of two photons of the pulse laser ($1080/2 = 540 \text{ nm}$ corresponding to 2.3 eV) changes are not unexpected.

The experiment is performed with polarized light (532 nm), at first with analyser parallel to the incoming beam (\parallel), at second with crossed polarizers (\perp). The light used by the laser is originally already linearly polarized, but the beam guide contains an optical fibre on the illumination side that partially depolarizes the light. Therefore, a polarizer is set to maximum intensity of the strongest raman peak. This setting of the polarizer is given the designation zero degree (\parallel , 0°). The measurements of the raman light are then analysed with the analyser parallel (\parallel , 0°) and perpendicular (\perp , 90°) to this position in order to gain initial insights into any anisotropy of the sample and corresponding changes during a possible photochemical reaction. When exposed to linearly polarized light, it turned out that mostly an attenuation of the response intensity is found in the middle of the square, e.g. at wavenumbers $1441\text{-}1476 \text{ cm}^{-1}$ (marked in cyan) as to be seen in Figure 6. It can be concluded that at this position, which is used to adjust the focus, an increased amount of light causes bleaching by destroying the underlying molecular bonds. While the exposed center is usually subject to a slight to severe loss of intensity after $\approx 4 \text{ h}$ (labeled L) and $\approx 18 \text{ h}$ (labeled H), there are also spectral regions in which this is reversed. This applies to the rising or falling flanks of the region of the vinyl bond by 1630 cm^{-1} and the carbonyl region by 1740 cm^{-1} . Since it has already been shown that with increasing exposure to light at 532 nm, the vinyl concentration decreases overall, this slight increase suggests a chemical change in the environment of the still existing vinyl bonds. Accordingly, the local concentrations of the various carbonyl bonds also change. The very probable involvement of dissolved atmospheric oxygen has already been pointed out.

The experiment is performed with polarized light (532 nm), at first with analyser

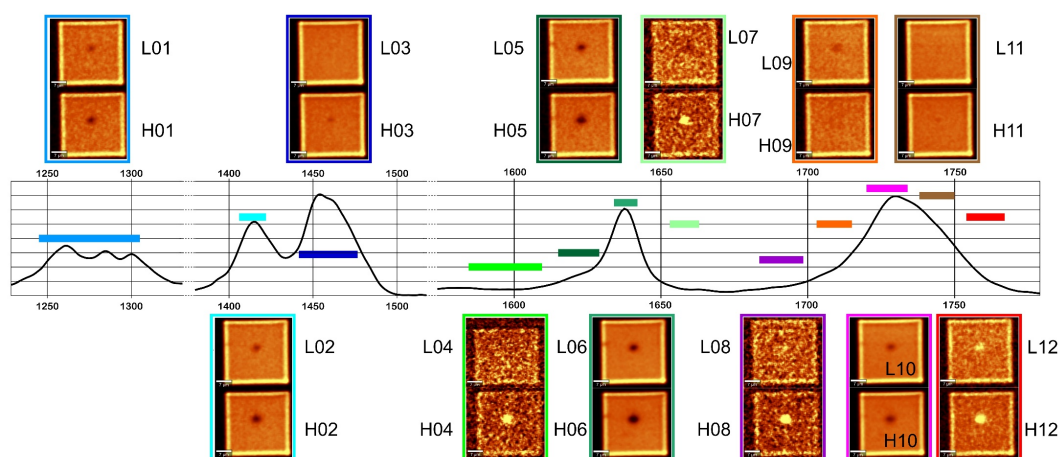


Figure 6: Result of hyperspectral imaging of the artefact at the position dedicated for raman spectroscopy, measured with grating T3 (1 cm^{-1}). Incoming laser beam at 0° (polarizer position), analyser at 0° (\parallel). The laser load is described by the two letters L and H (L = low, H = high), L means a period of a max. 4 h, which is required for focusing, distance optimizing to maximum raman yield and measurement of spectra. H corresponds to an additional exposure time of 14 h at the identical position of the sample. The raman spectrum in arbitrary units is an average spectrum of an unpolarized measurement of the hole area as a guide to the eye. The color-coded sections in the spectrum were selected according to the distinctness of the exposure results. The abscissa was interrupted twice for the purpose of clarity of the representation at sections without spectral information.

parallel to the incoming beam (\parallel), at second with crossed polarizers (\perp). The light used by the laser is originally already linearly polarized, but the beam guide contains an optical fibre on the illumination side that partially depolarizes the light. Therefore, a polarizer is set to maximum intensity of the raman spectrum. This setting of the polarizer is given the designation zero degree. The measurements of the raman light are then analysed with the analyser parallel (0°) and perpendicular (90°) to this position in order to gain initial insights into any anisotropy of the sample and corresponding changes during a possible photochemical reaction. When exposed to linearly polarized light, it turned out that mostly an attenuation of the response intensity is found in the middle of the square, e.g. at wavenumbers $1441 - 1476\text{ cm}^{-1}$ (marked in cyan) as to be seen in Figure 6 It can be concluded that at this position, which is used to adjust the focus, an increased amount of light causes bleaching by destroying the underlying molecular bonds. While the exposed center is usually subject to a slight to severe loss of intensity after $\approx 4\text{ h}$ (labeled L) and $\approx 18\text{ h}$ (labeled H), there are also spectral regions in which this is reversed. This applies to the rising or falling flanks of the region of the vinyl bond by 1630 cm^{-1} and the carbonyl region by 1740 cm^{-1} . Since it has already been shown that with increasing exposure to light at 532 nm , the vinyl concentration decreases overall, this slight increase suggests a chemical change in the environment

of the still existing vinyl bonds. Accordingly, the local concentrations of the various carbonyl bonds also change. The very probable involvement of dissolved atmospheric oxygen has already been pointed out.

Comparing these results with measurements with crossed polarizers (Pol 0°, Ana 90°) gives the same picture. As expected, the raman intensity is smaller with crossed polarizers, so only the signal/noise ratio is smaller. Further differences are not detectable, which is why an evaluation of the local degree of polarisation, e.g., is not carried out. In summary, it can be said that, at least under the parameters chosen so far for the printing of the test artefact, no reorientation of bonds occurred during ageing in visible light. This may be related to the fact that only the really last vinyl groups were able to react, and these are already so anchored in the network that only little rotation, i.e., reorientation, is needed.

2.3. Qualification

With the described geometrical features an insight in the relationship between photoresist and its adhesion on the substrate can be gained. The adhesion of rods and thin walls to the substrate can be investigated. The criterion derives from the fact that if the adhesion between the structure and the substrate is too low, the individual bar will collapse or fall over. This can be seen in Figure 7. All rods smaller than a predefined size of 2 μm collapsed with the used parameter set of the fabrication process. Similar behaviour in the collapse of the thin walls attached to the main structure can be seen in Figure 8, where the mechanical strength appears to be too low. The thin walls are deformed by mutual attraction but are still attached to the substrate.

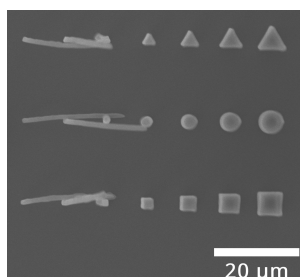


Figure 7: SEM image of Rod feature (#4) directly on substrate, partially collapsed are smallest three rods of each geometry, SZ2080, 6 mW, d_h 0.2 μm , d_z 0.4 μm , 3DPoli sliced

A partial analysis of the test artifact can be done by light microscopy. We evaluated multiple test artifacts with light microscopy, confocal laser scanning microscopy and a digital light microscope. Collapsed features as previously shown can also be examined with these methods (not shown). An overview image of a test artifact is given in Figure 9. As already described above, size and symmetry of the immersion indicator helps to help to assess the Z-position of the first slicing plane and to predict the achievable adhesion to the substrate. An immersion indicator evaluated by light microscopy is shown in

First of its kind: A test artifact for Direct Laser Writing

15

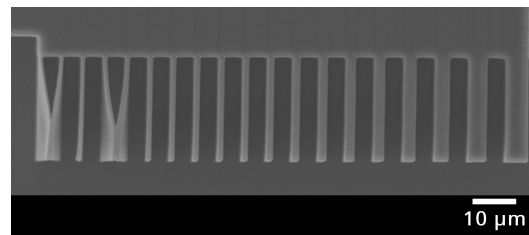


Figure 8: SEM image of Thin Walls (#8) attached to bulk, partially collapsed, SZ2080, 6 mW, d_h 0.2 μm, d_z 0.2 μm, 3DPoli sliced, Scale bar 10 μm

Figure 10. In this case it can be estimated that the first Z-layer is about 0.39 μm below the glass plane.

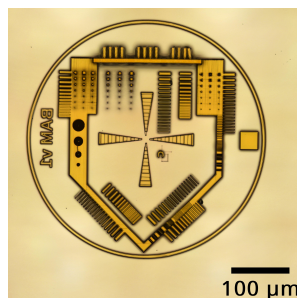


Figure 9: Light Microscopy image of a test artifact SZ2080, 8 mW, d_h 0.2 μm, d_z 0.4 μm

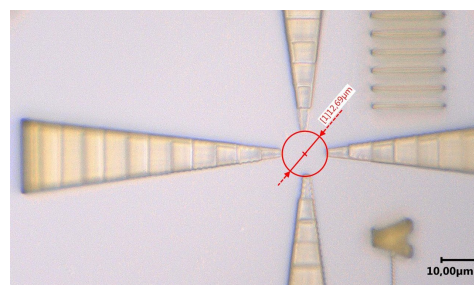


Figure 10: Digital Microscopy Image of the immersion indicator with a distance between the start of the immersion indicators of 12.69 μm and a calculated intrusion depth of 0.39 μm. SZ2080, 12 mW, d_h 0.2 μm, d_z 0.4 μm

The test artifact was further fabricated with OrmoComp photoresist, which is shown in the Supplementary Information. The test artifact can naturally also be fabricated on different substrates like silicon wafers, poly ethylenterephtalate foil or a steel disc. The different substrate properties like roughness, reflectivity or adhesion with photoresists influence the test artifacts quality.

2.4. Adapting for different optics

3.6 The data presented is based on the use of an oil immersion lens with a numerical aperture of 1.4, but working with air lenses is also possible. Air lenses have a smaller numerical aperture and therefore the voxel size is stretched along the XY axis and by a larger factor in the Z axis, as shown by [37]. The test artifact should therefore be scaled independently for XY and Z axis. The hatching and slicing distances have also to be adjusted to ensure a reasonable voxel overlap and fabrication times. The energy distribution in the focal area of the objective estimated via gaussian beam can be a guideline to estimate those values. To fabricate the test artifact with an 0.95 NA objective we used a scaling by a factor of 1.5 in XY and 2 in Z, resulting in a diameter of 612 μm and a height of 60 μm . Hatching d_h and slicing d_z distances were set at 0.4 μm and 0.6 μm respectively. The resulting structure can be seen in Figure 11. The measured feature sizes are shown in Table 3. It has to be noted that due to the different scaling in the spatial directions the angles ,e.g., of the cone feature, are distorted.

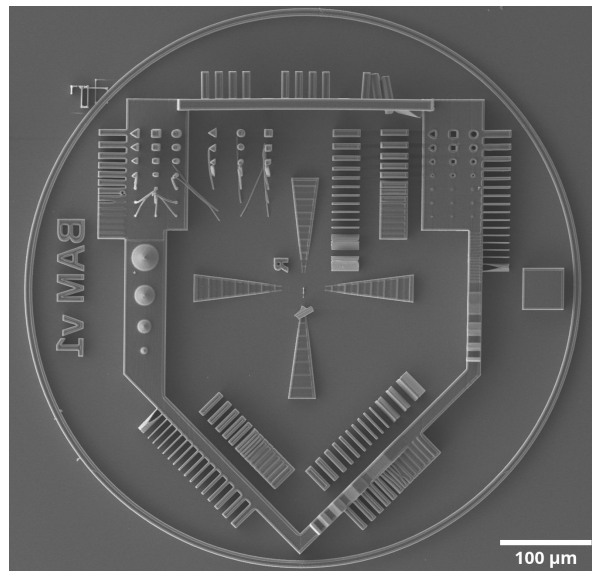


Figure 11: SEM image of a test artifact fabricated with a 0.95 NA air objective, SZ2080, 12 mW, 7000 $\mu\text{m}/\text{s}$, 612 μm diameter, 60 μm height, d_h 0.6 μm , d_z 0.8 μm , 3DPoli sliced

2.5. Limitations

The test artefact is not one-to-one applicable for very flexible materials or combinations of photoresist and photoinitiator where photopolymerisation is done with a large voxel size. The current spacing between the individual features must then be changed to obtain a benchmark also for such photoresists.

Furthermore, currently individual features cannot be extracted and individually fabricated from the current test artifact model. This would be beneficial for requirements, where only a certain set of features is needed. Such an approach would

First of its kind: A test artifact for Direct Laser Writing

17

Table 3: Observed features and results from the analysed test artifact fabricated with an 0.95NA objective, only minimal feature sizes are given

Feature	Results	Comment
Thin Walls		
on substrate	6 walls collapsed, min. 1.9 μm	no difference between 0° and 45°
attached to bulk	2 walls collapsed, min. 1.7 μm	
Gaps		
on substrate	min. 2.1 μm	no difference between substrate or bulk at 45°
attached to bulk	min. 1.4 μm	
45°	min. 2.1 μm	
Rods		
on substrate	3 attached, min. 5.4 μm	
on bulk	4 attached, min. 3.5 μm	
Holes	4 open holes, min. diameter 2.2 μm	
Z spacing feature	Attached: 8 Distorted: 3 Gone: 1	min. Z distance: 6.5 μm

lower the fabrication time, while still working with a predefined set of features from a known test artifact.

3. Practical applications

3.1. Influence of Slicers on Test artifact

4.2 As an application example for the presented test artefacts, we want to investigate the influence of two different slicers on the above mentioned properties of the test artefacts. Slicers are an integral part of DLW production technology. Slicers developed with DLW in mind have been proposed in the literature with a sub-regional slicing approach by Park [38] and an adaptive slicing method using the tilted voxel by Zheng [39].

However both methods are currently not available either open-source or as part of the used DLW setup itself. A review on the considerations for slicing approaches in DLW can be found in the work of Zhou [40].

The shape and geometric accuracy as well as the mechanical or optical properties of the resulting structure are partially depending on the tool path the slicing software generates from the given 3D model as well as the parsed parameters. [41, 42]

For example, a cube with a side length of 4 μm cannot be cut with evenly distributed lines at a hatching distance of 0.3 μm . The lines must be distributed either more densely or more sparsely. This changes the overlap between the voxels and therefore the mechanical properties also change. For SZ2080, it has also been shown [26] that the time between each manufactured line or cut distorts the shape of a structure.

The 3DPoli software provided with the used DLW machine has an integrated slicing component, where hatching and slicing distance as well as the option for an outer contour

line can be set. GCode from other slicers can be imported into 3DPoli via a command. For comparison, we used the 3DPoli slicer and Cura v6.11, an open-source slicer, which is mainly developed with fused-deposition modelling (FDM) printers in mind. The Cura slicer is not optimized for DLW technology. The sizes given in the GCODE must be divided by 1000 to get from the sizes used in Cura (millimeters) to the micrometers in DLW manufacturing.

The main dissimilarity between the slicers is the way an objects slice is filled with tool paths to be moved along. In Figure 12 the difference between the two slicing approaches can be seen. In Cura, we use 4 outer shells and 100% fill to fully polymerize a slice, alternating hatch lines along the X/Y axis for each slice. For features oriented at a 45° angle to the XY axis, both slicers also use a different approach. The 3DPoli slicer uses short lines along the X/Y axis, while the Cura slicer moves the ray along the contour line of the feature and only switches to perpendicular hatch lines above a certain geometric threshold

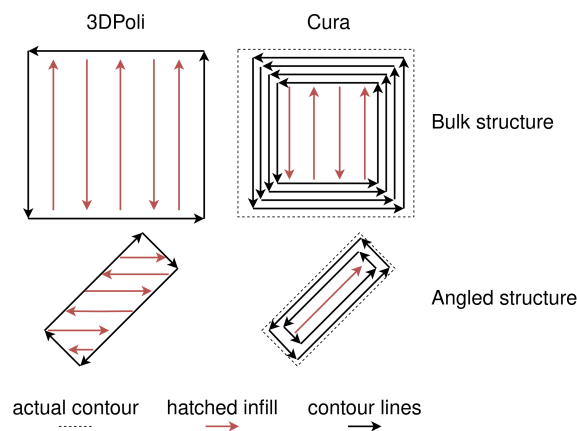


Figure 12: Simplified Illustration for the chosen beam paths of 3DPoli and Cura slicer, red hatched infill and black arrows outer contour lines shown for a simple cubic geometry and a 45° angled thin wall

The chosen beam path by the slicer has an impact on the resulting geometrical accuracy. In Figure 13 a partial enlargement because of a missing beam width offset is shown.

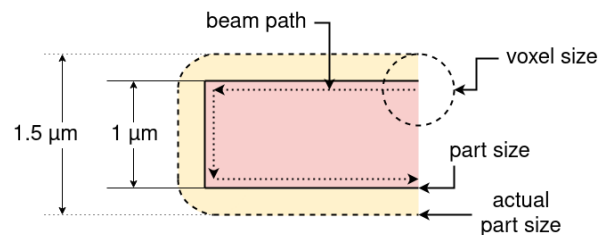


Figure 13: Schematic illustration of connection between voxel size, beam path and resulting shape

The parameters for hatching, slicing as well as for laser power and velocity have not been changed to enable comparability of both slicers. The additionally used parameter set can be seen in Table 4.

Table 4: Settings in 3DPoli and Cura Slicer

Slicer	3DPoli	Cura
Parameter	Contour Shell before Hatching Contour Shell = True	0.2 mm Layer Height 0.2 mm Nozzle Size Infill Line Directions = [0, 90] Wall Line Count = 4 Print Thin Walls = True

The following parameter set was used for both slicers: a laser power of 8 mW and 12 mW respectively, beam velocity 7000 $\mu\text{m}/\text{s}$, a hatching distance d_h 0.2 μm and a slicing distance of d_z 0.4 μm . To compare the test artifacts the features thin walls, gaps and rods and holes features were measured via SEM. In Figure 14 the measured sizes are compared between the two slicers. Ideally, the measured sizes correspond to the nominal size, i.e. the size of the feature in the model.

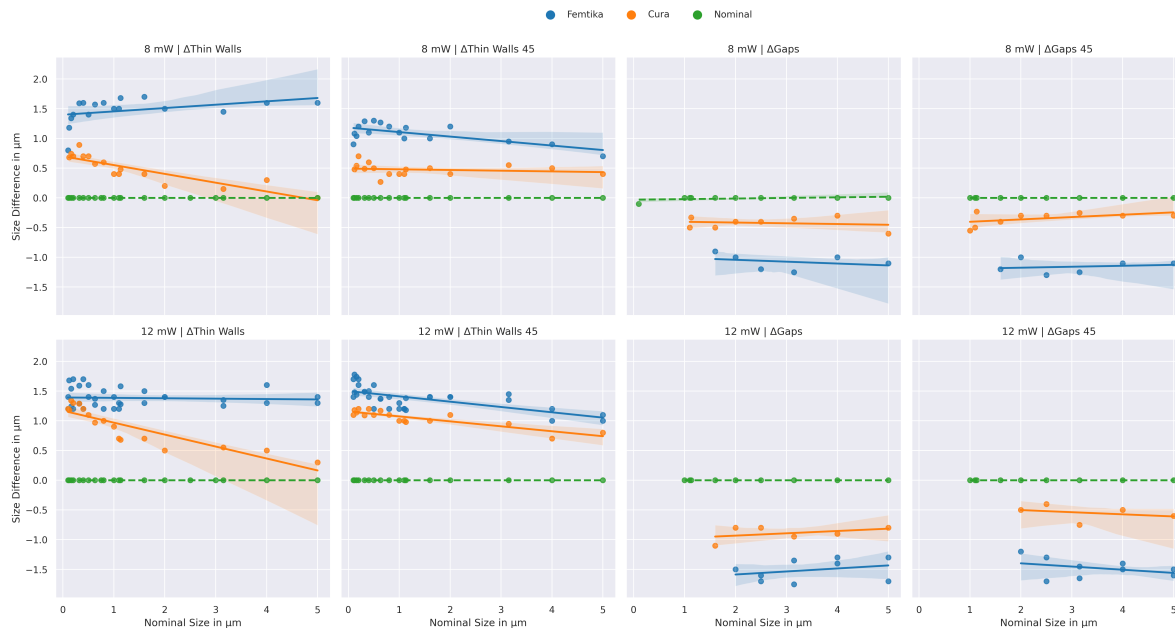


Figure 14: Deviation from Nominal size for Thin Walls and Gaps features at different laser powers, a 95% confidence interval is given for the fit line

The so-called nominal sizes are given as dashed lines. With both slicers the features are fabricated either too large or, in the case of the gap feature, the distance between the adjacent walls is too narrow and the gap closes too early. If the line of the measured

sizes runs parallel to the nominal sizes a general offset can be applied to get a correct size.

For the thin walls features sliced with 3DPoli the measured sizes were higher than Cura sliced ones. The difference between the two slicers was lower for the higher laser power. Thin walls with 45° alignment showed a more similar behaviour where the 3DPoli sliced walls were larger but with a smaller offset. The lower wall thicknesses for Cura sliced walls can be partially explained by the internal offset for the squished filament under nozzle of a FDM printer. However, as the Nozzle Size in the parameters was set to 0.2 mm, the offset is only 0.1 mm in the original GCODE or 0.1 μm in DLW process. For the thin walls feature the Cura slicer showed a slightly different behaviour, where the offset partially decreased with increasing size of the thin walls. For larger dimensions, the real dimensions of the thin walls are thus closer to the values of the test artifact.

In Figure 15 the measured sizes of thin wall features attached to the bulk body are shown. A similar behaviour as previously seen with the non-attached walls can be noticed. Cura sliced features have a higher geometrical accuracy too but the general feature size for walls attached to a bulk body was higher. This observation can possibly be attributed to a high acceleration of the jet along the contour, which is then suddenly stopped in order to produce the adjacent wall element, which is perpendicular to the contour of the bulk material body.

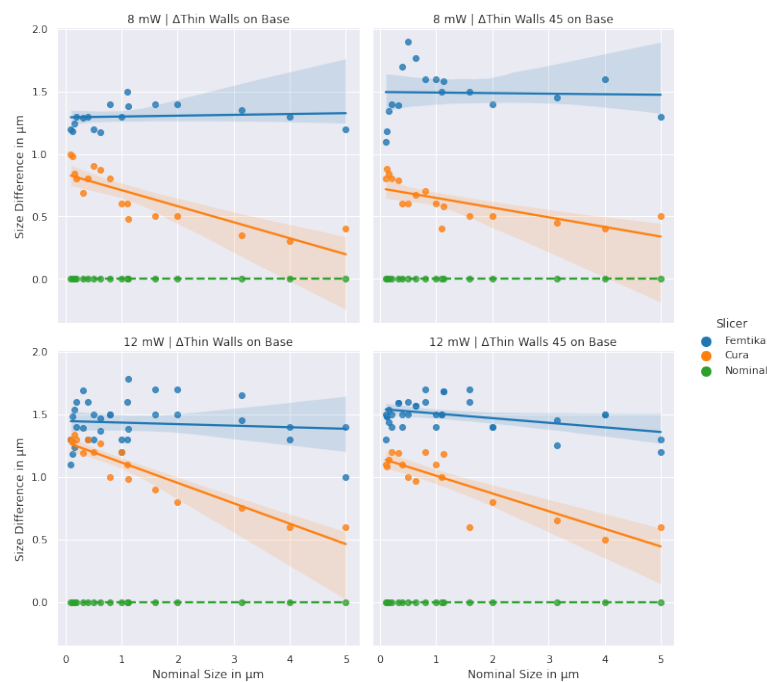


Figure 15: Deviations of feature sizes for Thin Walls that are attached to the bulk body

In Figure 16 a similar behaviour is shown for the gaps that are attached to the bulk body. Similar to the features shown previously, the geometric accuracy is higher for the

test artefacts sliced with Cura. At 8 mW Laser Power the Cura-sliced sizes are nearly identical to the nominal sizes but a higher scattering is noted as shown.

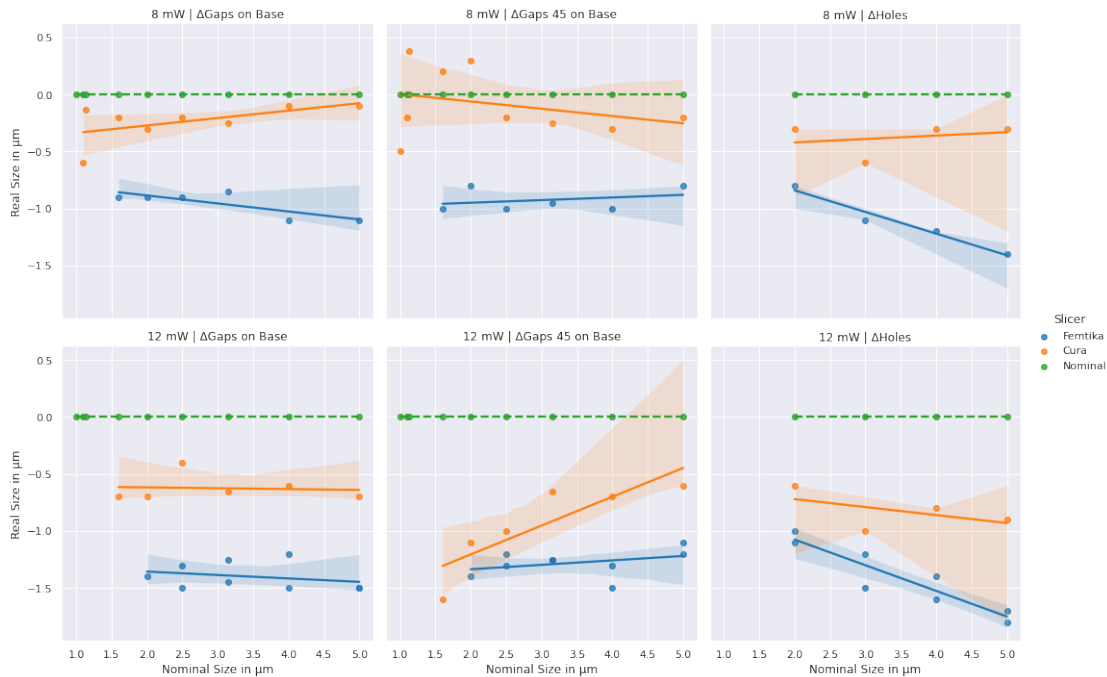


Figure 16: Deviations of feature sizes for Holes feature and Gaps that are attached to the bulk body

The produced test artefacts can also be compared qualitatively. A comparison of the cone feature between both slicers can be seen in Figure 17a and Figure Figure 17c. The 3DPoli feature has a pronounced stair-step effect and a small dent on the left side, possibly due to similar starting points for each slice. On the cone cut in Cura, the staircase effect is less visible, but a prominent line was observed on the right side. The Cura slice here shows its origin from the FDM process, as we assume that this line comes from the seam line and a pronounced wiping process performed to remove unwanted molten filament from the nozzle. This defect can probably be eliminated by a further fine tuning of the Cura parameter set.

To compare the general quality of the difference between the fabricated structures Figure 17c, 3DPoli-sliced, and Figure 17d, Cura-sliced, a tilted view on the Z-spacing feature was picked. On the 3DPoli sliced structure on the left pillar side shows a reproducible slight bending towards the middle, which we attribute to the shrinkage of the SZ2080 photoresist. The 3DPoli sliced structure shows a very high sharpness and with no visible deformations in on the bulk surface. The bars on the right side are heavily merged with the beam, whereas the more left ones are only slightly attached. It has to be noted that the top surface of the top bar seems to be dented above each of the pillars which could indicate incomplete curing of the photoresist even though the same laser power and velocity as well as hatching distance was chosen. We assume a problem in the interpretation of the GCODE in the 3DPoli software. The structure sliced with

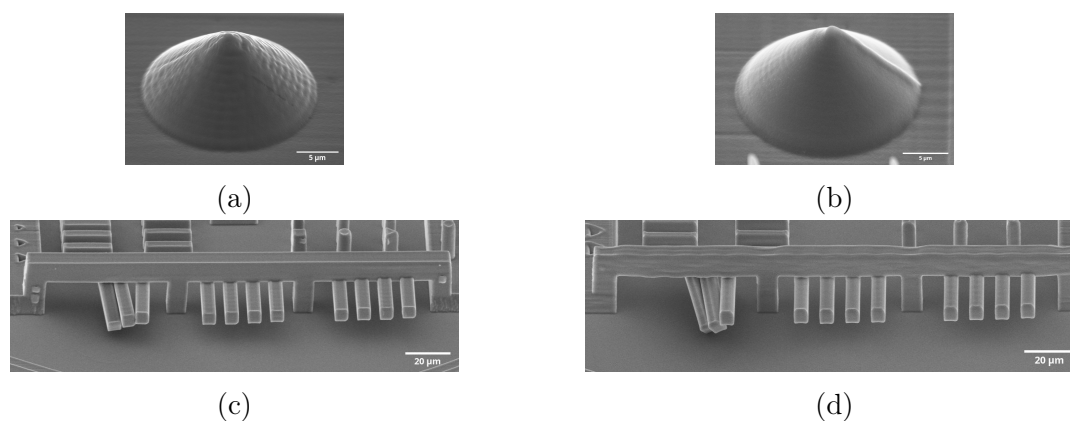


Figure 17: SEM images of cone and Z spacing features sliced with (a), (c) 3DPoli or (b), (d) Cura respectively

Cura on the other hand had a wobbly surface with unsharp edges. Interestingly a similar amount of attached bars can be found on both structures as the intrusion of beam and bar into is similar. This is an indication that laser power, hatching and slicing distances play a more important role than the slicer used.

Design parameters can be calculated from the collected geometric measurements by subtracting the offset obtained from the measurement of each feature. These design parameters apply to the same set of parameters with which the test specimen was manufactured. The required offsets in the Z-direction can only be estimated with this test artefact, as no special function for construction parameters parallel to the substrate has been implemented.

4. Conclusion and Outlook

With its unique manufacturing technology and the outstanding resolution DLW offers a wide range of applications. To build a resilient quality infrastructure is therefore needed to broaden the acceptance of DLW as a reliable fabrication technique. The shown test artifact was shown to work on different substrates as well as in a comparison with different laser power/velocity pairings.

In a, to our knowledge, first comparison of two different slicers with DLW, the impact of the slicing strategy was examined. Both the slicer from 3DPoli and Cura show individual strengths. This underlines the need to evaluate the slicing strategy individually for each object to be printed. Whereas feature sizes were generally lower with Cura, the optical fabrication quality with the 3DPoli slicer was higher. A fast forward way to obtain minimal wall sizes and gap distances is possible with the test artifact. An object fabricated with construction parameters derived from the test artifact further strengthened the point for a common test artifact in DLW.

Furthermore, investigations showed that the degree of curing can be determined on the basis of the raman signal of the vinyl group and that the presence of oxygen

REFERENCES

23

reduces the efficiency of the formation of a network via the vinyl groups. Information of this kind makes it possible to compare writing processes with different parameters and predict the durability and dimensional stability of structures for micro-optical and micro-mechanical applications. What happens during light-curing, however, is a further increase in density due to the accompanying shrinkage process. A test structure whose shape changes in daylight has only limited durability and usefulness. However, a simple post-curing with visible light could solve the problem, and this would also make optical and mechanical microstructures more stable. It is planned to carry out a further investigation of this post-curing with light on suitable geometries, with AFM on stiffness and surface adhesion [43], as well as to make measurements of the resonance frequency of beams to determine the bending modulus [44]. In contrast to thermal post-curing, the geometric dimensions change only slightly because the structures do not expand before the curing leads to shrinkage.

The test artifact we presented in this work is a first of its kind. Similar to the evolution of test artifacts for metal and polymer additive manufacturing techniques our DLW artifact is not matured yet. We are curious for suggestions to improve the artifact further or to see other designs in the future.

References

- [1] Tommaso Baldacchini, **editor**. *Three-dimensional microfabrication using two-photon polymerization. 2 edition*. Micro & Nano Technologies. Norwich, CT: William Andrew Publishing, **october** 2019.
- [2] Xiaoqin Zhou, Yihong Hou **and** Jieqiong Lin. ?A review on the processing accuracy of two-photon polymerization? **in** *AIP Advances*: 5.3 (2015), **page** 030701.
- [3] Attilio Marino **and others**. ?A 3D Real-Scale, Biomimetic, and Biohybrid Model of the Blood-Brain Barrier Fabricated through Two-Photon Lithography? **in** *Small*: 14.6 (2018), **page** 1702959.
- [4] Enrico Domenico Lemma **and others**. ?Studying cell mechanobiology in 3D: the two-photon lithography approach? **in** *Trends in biotechnology*: 37.4 (2019), **pages** 358–372.
- [5] Amelie Erben **and others**. ?Precision 3D-printed cell scaffolds mimicking native tissue composition and mechanics? **in** *Advanced healthcare materials*: 9.24 (2020), **page** 2000918.
- [6] Timo Gissibl **and others**. ?Two-photon direct laser writing of ultracompact multi-lens objectives? **in** *Nature photonics*: 10.8 (2016), **pages** 554–560.
- [7] Linas Jonušauskas **and others**. ?Optically clear and resilient free-form μ -optics 3D-printed via ultrafast laser lithography? **in** *Materials*: 10.1 (2017), **page** 12.
- [8] Winthrop F Gillis **and others**. ?Carbon fiber on polyimide ultra-microelectrodes? **in** *Journal of neural engineering*: 15.1 (2018), **page** 016010.

REFERENCES

24

- [9] Raffaele Di Giacomo **and others**. ?Deployable micro-traps to sequester motile bacteria? *in Scientific reports*: 7.1 (2017), **pages** 1–8.
- [10] Anna V Nielsen **and others**. ?3D printed microfluidics? *in Annual Review of Analytical Chemistry*: 13 (2020), **pages** 45–65.
- [11] Felix Ströer **and others**. ?Ultrafast 3D high precision print of micro structures for optical instrument calibration procedures? *in Additive Manufacturing*: 18 (2017), **pages** 22–30.
- [12] Matthias Eifler **and others**. ?Calibration sample for arbitrary metrological characteristics of optical topography measuring instruments? *in Optics Express*: 26.13 (2018), **pages** 16609–16623.
- [13] A Matei **and others**. ?Two photon polymerization of ormosils? *in AIP Conference Proceedings*: **volume** 1278. 1. American Institute of Physics. 2010, **pages** 843–851.
- [14] Jin-Feng Xing, Mei-Ling Zheng **and** Xuan-Ming Duan. ?Two-photon polymerization microfabrication of hydrogels: an advanced 3D printing technology for tissue engineering and drug delivery? *in Chemical Society Reviews*: 44.15 (2015), **pages** 5031–5039.
- [15] Jan Torgersen **and others**. ?Hydrogels for two-photon polymerization: a toolbox for mimicking the extracellular matrix? *in Advanced Functional Materials*: 23.36 (2013), **pages** 4542–4554.
- [16] Johanna C Säger **and others**. ?First time additively manufactured advanced ceramics by using two-photon polymerization for powder processing? *in Open Ceramics*: 4 (2020), **page** 100040.
- [17] Mateusz Dudziak **and others**. ?Long-Time Behavior of Surface Properties of Microstructures Fabricated by Multiphoton Lithography? *in Nanomaterials*: 11.12 (2021). ISSN: 2079-4991. URL: <https://www.mdpi.com/2079-4991/11/12/3285>.
- [18] Shawn Moylan **and others**. ?An additive manufacturing test artifact? *in Journal of research of the National Institute of Standards and Technology*: 119 (2014), **page** 429.
- [19] HC Taylor, EA Garibay **and** RB Wicker. ?Toward a common laser powder bed fusion qualification test artifact? *in Additive Manufacturing*: 39 (2021), **page** 101803.
- [20] Amit J. Lopes **and others**. ?Comparison of ranking models to evaluate desktop 3D printers in a growing market? *in Additive Manufacturing*: 35 (2020), **page** 101291. ISSN: 2214-8604. URL: <https://www.sciencedirect.com/science/article/pii/S2214860420306631>.
- [21] Sourabh K Saha **and others**. ?Effect of proximity of features on the damage threshold during submicron additive manufacturing via two-photon polymerization? *in Journal of Micro and Nano-Manufacturing*: 5.3 (2017).

REFERENCES

25

- [22] Sönke Steenhusen, Sebastian Hasselmann **and** Gerhard Domann. ?Strategies for rapid and reliable fabrication of microoptical structures using two-photon polymerization? **in***Advanced Fabrication Technologies for Micro/Nano Optics and Photonics X*: by editor Georg von Freymann, Winston V. Schoenfeld **and** Raymond C. Rumpf. **volume** 10115. International Society for Optics **and** Photonics. SPIE, 2017, 101150S.
- [23] Ada-Ioana Bunea **and others**. ?Micro 3D Printing by Two-Photon Polymerization: Configurations and Parameters for the Nanoscribe System? **in***Micro*: 1.2 (2021), **pages** 164–180. ISSN: 2673-8023.
- [24] Severin Schweiger **and others**. ?Characterization of two-photon-polymerization lithography structures via Raman spectroscopy and nanoindentation? **in***Journal of Optical Microsystems*: 2.3 (2022), **page** 033501.
- [25] Jens Bauer **and others**. ?Programmable Mechanical Properties of Two-Photon Polymerized Materials: From Nanowires to Bulk? **in***Advanced Materials Technologies*: 4.9 (2019), **page** 1900146.
- [26] Sven Fritzsche **and others**. ?Shape deviations of DLW microstructures in dependency of fabrication parameters? **in***Journal of Micromechanics and Microengineering*: 31.12 (october 2021), **page** 125002.
- [27] Shawn Moylan **and others**. *A review of test artifacts for additive manufacturing*. US Department of Commerce, National Institute of Standards **and** Technology, 2012.
- [28] Hong-Seok Byun **and** Kwan Heng Lee. ?Design of a new test part for benchmarking the accuracy and surface finish of rapid prototyping processes? **in***International Conference on Computational Science and its Applications*: Springer. 2003, **pages** 731–740.
- [29] Edvinas Skliutas **and others**. ?Polymerization mechanisms initiated by spatio-temporally confined light? **in***Nanophotonics*: (2021).
- [30] Frank Burmeister **and others**. ?Materials and technologies for fabrication of three-dimensional microstructures with sub-100 nm feature sizes by two-photon polymerization? **in***Journal of Laser Applications*: 24.4 (2012), **page** 042014.
- [31] Linas Jonušauskas **and others**. ?Mesoscale laser 3D printing? **in***Optics express*: 27.11 (2019), **pages** 15205–15221.
- [32] *ISO 3:1973 Preferred numbers — Series of preferred numbers*. Norm. 1973. URL: <https://www.iso.org/standard/3564.html>.
- [33] Samuel Obi. ?Replicated optical microstructures in hybrid polymers: Process technology and applications? phdthesis. Université de Neuchâtel, 2006.
- [34] Jan Rys **and others**. ?Locally addressable material properties in 3D micro-architectures? **in***Extreme Mechanics Letters*: 28 (2019), **pages** 31–36. ISSN: 2352-4316.

REFERENCES

26

- [35] T. Visser **and** J. H. van der Maas. ?Systematic interpretation of Raman spectra of organic compounds. III—carbonyl compounds? **in** *Journal of Raman Spectroscopy*: 7.3 (1978), **pages** 125–129.
- [36] Josephine Anne Ellwood. *Raman band intensities of thioethers and thiols*. University of London, Royal Holloway **and** Bedford New College (United Kingdom), 1989.
- [37] Linas Jonušauskas, Saulius Juodkazis **and** Mangirdas Malinauskas. ?Optical 3D printing: bridging the gaps in the mesoscale? **in** *Journal of Optics*: 20.5 (april 2018), **page** 053001.
- [38] Sang Hu Park **and others**. ?Subregional slicing method to increase three-dimensional nanofabrication efficiency in two-photon polymerization? **in** *Applied Physics Letters*: 87.15 (2005), **page** 154108.
- [39] Xu Zheng **and others**. ?An adaptive direct slicing method based on tilted voxel of two-photon polymerization? **in** *The International Journal of Advanced Manufacturing Technology*: 96.1 (2018), **pages** 521–530.
- [40] Xiaoqin Zhou, Yihong Hou **and** Jieqiong Lin. ?A review on the processing accuracy of two-photon polymerization? **in** *Aip Advances*: 5.3 (2015), **page** 030701.
- [41] Albertas Žukauskas **and others**. ?Tuning the refractive index in 3D direct laser writing lithography: towards GRIN microoptics? **in** *Laser & Photonics Reviews*: 9.6 (2015), **pages** 706–712.
- [42] Qin Hu **and others**. ?The influence of printing parameters on multi-material two-photon polymerisation based micro additive manufacturing? **in** *Additive Manufacturing*: 51 (2022), **page** 102575. ISSN: 2214-8604.
- [43] Dorothee Silbernagl **and others**. ?Bulk chemical composition contrast from attractive forces in AFM force spectroscopy? **in** *Beilstein Journal of nanotechnology*: 12.1 (2021), **pages** 58–71.
- [44] Renata Fortini **and others**. ?Measurement of flexural rigidity of multi-walled carbon nanotubes by dynamic scanning electron microscopy? **in** *Fibers*: 8.5 (2020), **page** 31.

Supplementary Information

1. Test artifacts fabricated on different substrates

Objective: 1.4 NA oil immersion objective, Zeiss Plan-Apochromat 63x

Photoresist: SZ2080 + 1% 4,4'-bis(N,N-diethylamino) benzophenone photo initiator

Laser Power: 12 μm , Velocity: 7000 $\mu\text{m}/\text{s}$

Slicer: 3DPoli

Hatching/Slicing: 200nm

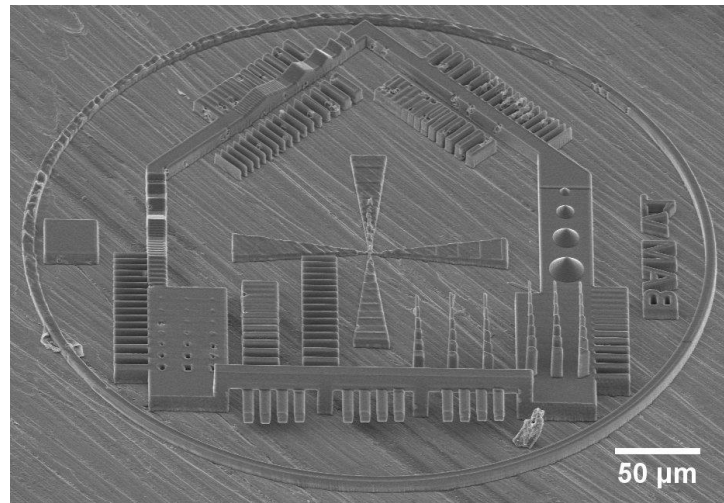


Figure 1: Steel substrate

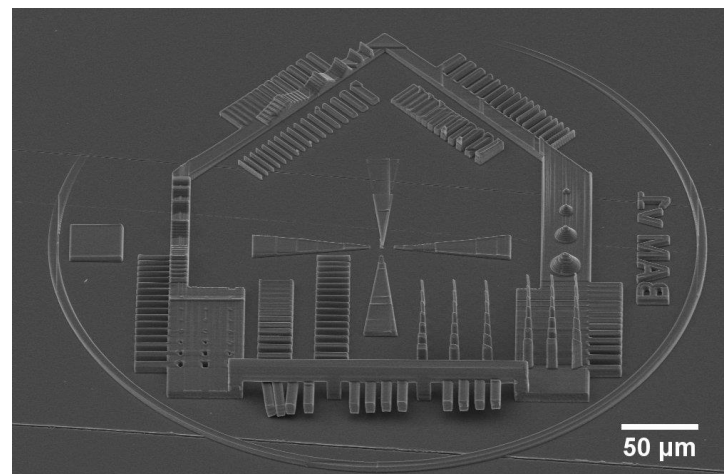


Figure 2: PET foil, 170 μm Thickness from Pützler Folien (Germany)

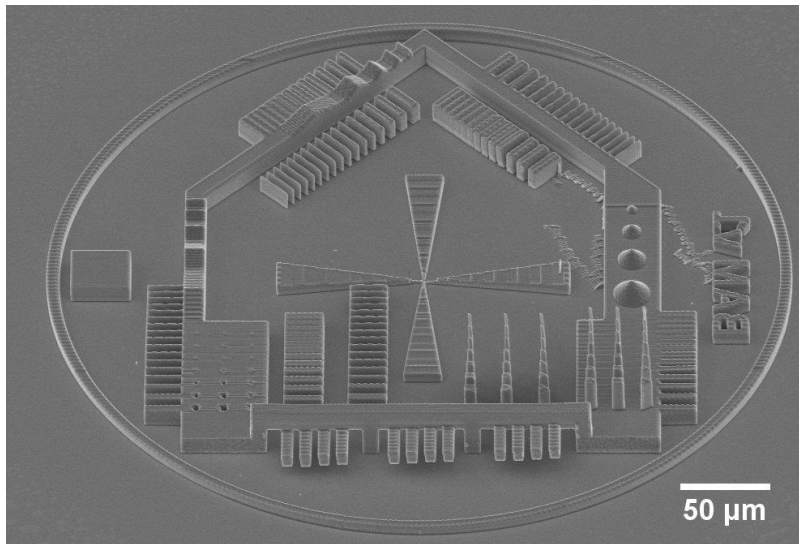


Figure 3: Si-Wafer

2. Test artifact fabricated with OrmoComp photoresist

Objective: 1.4 NA oil immersion objective, Zeiss Plan-Apochromat 63x

Photoresist: OrmoComp photoresist, obtained from Microresist GmbH/Germany

Laser Power: 18 μm, Velocity: 7000 μm/s

Slicer: 3DPoli

Hatching/Slicing: 200nm

